PNAS RESEARCH ARTICLE | ENGINEERING

Epitaxial $SrTiO_3$ films with dielectric constants exceeding 25,000

Zhifei Yang[a,b,1,2], Dooyong Lee[a,1,2], Jin Yue[a], Judith Gabel[c], Tien-Lin Lee[c], Richard D. James[d], Scott A. Chambers[e], and Bharat Jalan[a,2]

Edited by S. S. P. Parkin, Max Planck Institute of Microstructure Physics, Halle (Saale), Germany; received February 6, 2022; accepted April 29, 2022

$SrTiO_3$ (STO) is an incipient ferroelectric perovskite oxide for which the onset of ferroelectric order is suppressed by quantum fluctuations. This property results in a very large increase in static dielectric constant from ∼300 at room temperature to ∼20,000 at liquid He temperature in bulk single crystals. However, the low-temperature dielectric constant of epitaxial STO films is typically a few hundred to a few thousand. Here, we use all-epitaxial capacitors of the form *n*-STO/undoped STO/*n*-STO (001) prepared by hybrid molecular beam epitaxy, to demonstrate intrinsic dielectric constants of an unstrained STO (001) film exceeding 25,000. We show that the *n*-STO/undoped STO interface plays a critically important role not previously considered in determining the dielectric properties that must be properly accounted for to determine the intrinsic dielectric constant.

$SrTiO_3$ film | dielectric constant | ferroelectricity | antiferrodistortive transition

$SrTiO_3$ (STO) is an incipient ferroelectric or a quantum paraelectric oxide for which the ferroelectric transition is suppressed by quantum fluctuations (1). In bulk single crystals, this property has resulted in a giant increase in the static dielectric constant reaching up to ∼20,000 at liquid He temperature as well as a near constant value at $T \leq 4$ K (1–3). The high dielectric constant of STO at low temperature results in a large Bohr radius and small ionization energy; as a result, metallic conduction can be induced at a doping level as low as 8×10^{15} cm^{-3} (4, 5). Additionally, the large low-temperature dielectric constant has also been responsible for high electron mobility exceeding 22,000 $cm^2 \cdot V^{-1} \cdot s^{-1}$ owing to polarization shielding of scattering centers (6).

Another intriguing property of STO is its superconducting ground state that emerges at a low dopant concentration of $\sim 10^{17}$ cm^{-3} and persists up to 10^{20} cm^{-3} (5, 7). It has been argued that local stresses, leading to ferroelectric behavior, can enhance the superconducting transition temperature (T_c) in plastically deformed bulk STO single crystals (8). Epitaxial strain has also been shown to induce ferroelectricity in STO (9–12) and has resulted in a factor of 2 increase in T_c relative to unstrained doped STO (13). Furthermore, undoped STO undergoes a cubic-tetragonal antiferrodistortive (AFD) phase transition near 105 K upon cooling (2, 14). Some studies have suggested that the AFD phase transition suppresses the ferroelectric transition at high temperatures (15). Owing to the interplay between ferroelectricity and superconductivity (13, 16–19), these diverse aspects have renewed interest in the dielectric and ferroelectric properties of STO films.

Conductive oxides such as $SrRuO_3$ and metals like Ir, Pt, and Au are typically used as one or both of the top and bottom electrodes for STO dielectric studies (11, 20–23). The measured dielectric constants for STO films never exceed a few thousand at low temperature (20, 23–26) whereas bulk STO exhibits a value of ∼20,000 (1). However, Takashima et al. (27, 28) reported a bulk-like low-temperature dielectric constant of ∼25,000 in a pulsed-laser–deposited STO film using a structure consisting of $YBa_2Cu_3O_{7-\delta}$ as bottom and top electrodes and fabricated with the assistance of a chemical–mechanical planarization (CMP) method. In the more recent study (26), however, the same group showed a much lower dielectric constant of only 510 at 2 K using a homoepitaxial capacitor structure, suggesting the prior reports of high dielectric constants may likely be influenced by the heteroepitaxial nature of the structure or the defects introduced during the CMP process.

It remains therefore unclear whether the low dielectric constants are due to intrinsic or extrinsic defects in the STO films or due to interface-induced effects. It is thus important to understand why STO films appear to have lower dielectric constants and doing so may result in additional insights into the electronic properties of STO. To this end, we have grown all homo-epitaxial STO capacitor structures to systematically probe the intrinsic dielectric properties of STO thin films free from the influence of in-plane strain.

Significance

Semiconductor interfaces are among the most important in use in modern technology. The properties they exhibit can either enable or disable the characteristics of the materials they connect for functional performance. While much is known about important junctions involving conventional semiconductors such as Si and GaAs, there are several unsolved mysteries surrounding interfaces between oxide semiconductors. Here we resolve a long-standing issue concerning the measurement of anomalously low dielectric constants in $SrTiO_3$ films with record high electron mobilities. We show that the junction between doped and undoped $SrTiO_3$ required to make dielectric constant measurements masks the dielectric properties of the undoped film. Through modeling, we extract the latter and show that it is much higher than previously measured.

Author contributions: Z.Y., D.L., J.Y., and B.J. designed research; Z.Y., D.L., J.Y., J.G., T.-L.L., and S.A.C. performed research; Z.Y., D.L., J.Y., J.G., T.-L.L., R.D.J., S.A.C., and B.J. analyzed data; and Z.Y., D.L., and B.J. wrote the paper with feedback from all authors.

The authors declare no competing interest.

This article is a PNAS Direct Submission.

[1]Z.Y. and D.L. contributed equally to this work.

[2]To whom correspondence may be addressed. Email: bjalan@umn.edu, yang7001@umn.edu, or dylee@umn.edu.

This article contains supporting information online at http://www.pnas.org/lookup/suppl/doi:10.1073/pnas.2202189119/-/DCSupplemental.

Published June 2, 2022.

Results and Discussion

We use a hybrid molecular beam epitaxy (MBE) method to grow capacitor structures consisting entirely of STO (29, 30). Hybrid MBE has previously been shown to produce STO films with record high electron mobilities in excess of 30,000 $cm^2 \cdot V^{-1} \cdot s^{-1}$ at low temperature (31). We have grown different thicknesses of undoped STO (t = 100, 600, 800, 1,000 nm) on 0.5 wt% Nb-doped (001) STO substrates. We then grew 100 nm of doped STO films in situ for the top electrodes. Dy, Nd, and La were used as dopants and their concentration was fixed at ∼1 at.% of the A sites. Reflection high-energy electron diffraction (RHEED) was used to monitor the film growth dynamics and structure in situ. Typical intensity oscillations recorded at the start of the growth indicating layer-by-layer growth can be seen in Fig. 1*B*. A typical postgrowth RHEED pattern along the [100] direction is shown in Fig. 1 *B*, *Inset*. The streaky character of the Bragg rods reveals that the film surface is smooth. The high-resolution X-ray diffraction (XRD) scan in Fig. 1*A* shows the same Bragg angle for the thin films and the substrates, confirming the homoepitaxial nature and compositional accuracy of our samples.

To investigate the dielectric properties of these samples, we measured the complex impedance Z and calculated the permittivity based on the sample geometry. Complex impedance Z consists of two terms: a real resistance R and an imaginary reactance X such that $Z = R + iX$. The phase angle Θ is the phase shift between the AC voltage and current. For an ideal resistor, there is no reactance ($X = 0$) and $\Theta = 0°$. For an ideal capacitor, $R \approx 0$ and the reactance is capacitive with $\Theta = -90°$. The capacitive reactance (X_C) is related to the capacitance C by

$$|X_C| = \frac{1}{2\pi f C}, \qquad [1]$$

where f is the source frequency. However, there are no perfect capacitors and there is always some power dissipation. The resulting loss tangent is determined by

$$\tan\delta = \frac{R}{|X_C|} \qquad [2]$$

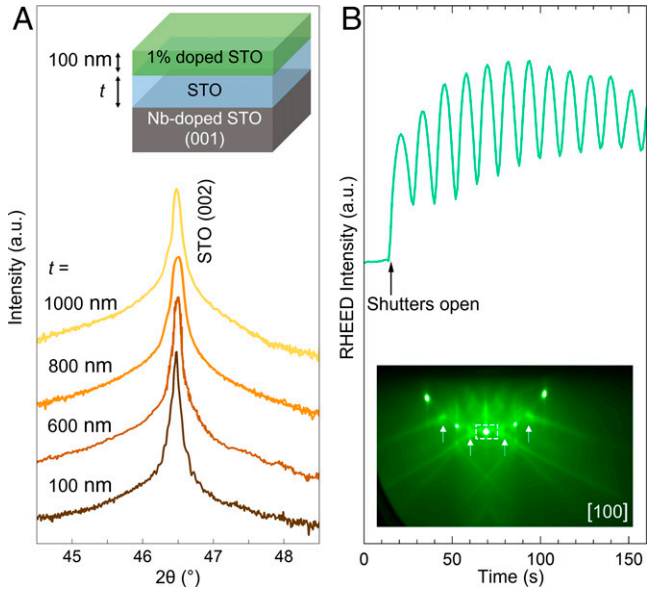

Fig. 1. Characterization of $SrTiO_3$ thin films during and after growth. (*A*) High-resolution, out-of-plane $2\theta - \omega$ XRD scans. *Inset* shows the sample structure. (*B*) Time-dependent RHEED intensity during a typical growth. *Inset* shows the postgrowth RHEED pattern along the [100] direction.

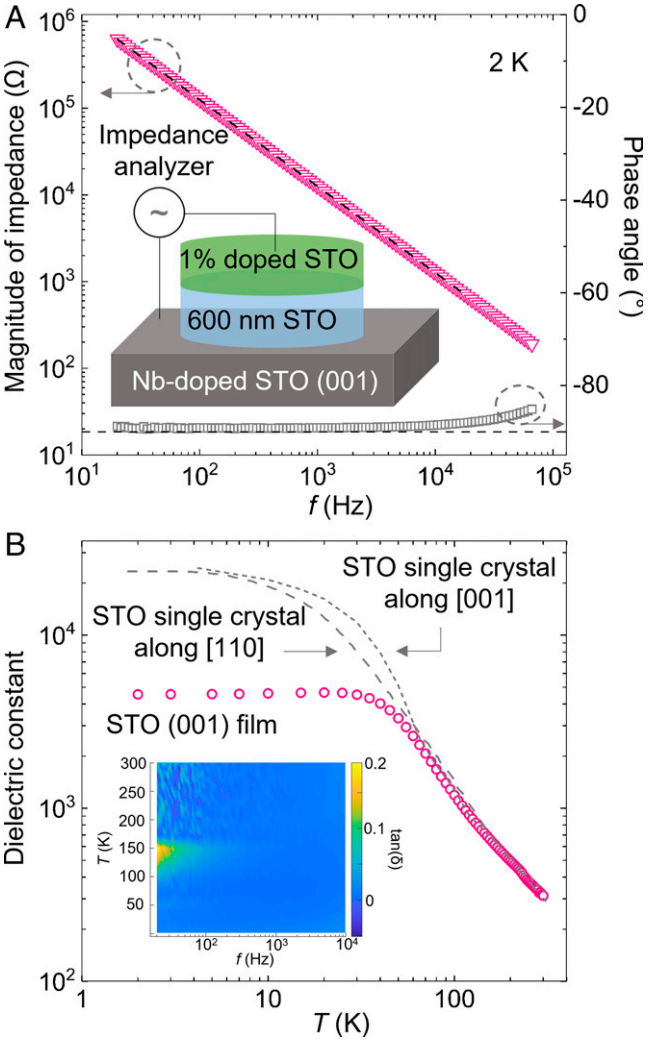

Fig. 2. Impedance measurements of homo-epitaxial 100-nm Nd-doped STO/600-nm STO/Nb-doped STO substrate. (*A*) Magnitude of complex impedance $|Z|$ and phase angle Θ as a function of frequency at 2 K. The dashed line is the linear fit to the data with the phase angle close to −90°. The device structure is shown in *Inset*. (*B*) Measured dielectric constant as a function of temperature for the same structure in addition to showing data from bulk STO single crystals (1,3) (dashed gray curve). *Inset* shows the loss tangent as a function of temperature and frequency.

and is typically used to characterize the dissipation. We used an impedance analyzer (Agilent E4990A) to perform frequency-dependent, complex impedance measurements and a Quantum Design PPMS Dynacool system for temperature control.

Fig. 2*A* shows the magnitude of the impedance $|Z|$ and phase angle Θ as a function of frequency at 2 K for a 100-nm Nd-doped STO/600-nm STO/Nb-doped STO (001) structure. The phase angle is very close to −90° over most of the frequency range, revealing a nearly ideal capacitor. Since $|X_C| \gg R$, $|Z| = |X_C|$. Using Eq. **1** in the frequency range where the phase angle is nearly −90°, we can determine the capacitance from the linear fit shown in Fig. 2*A* by using the relationship

$$\log(|X_C|) = -\log(2\pi f) - \log(C). \qquad [3]$$

Treating the structures as parallel-plate capacitors, we can extract the temperature dependence of the static dielectric constant κ from the measured capacitance by using

$$\kappa = \frac{C\ t}{\varepsilon_0\ A} \qquad [4]$$

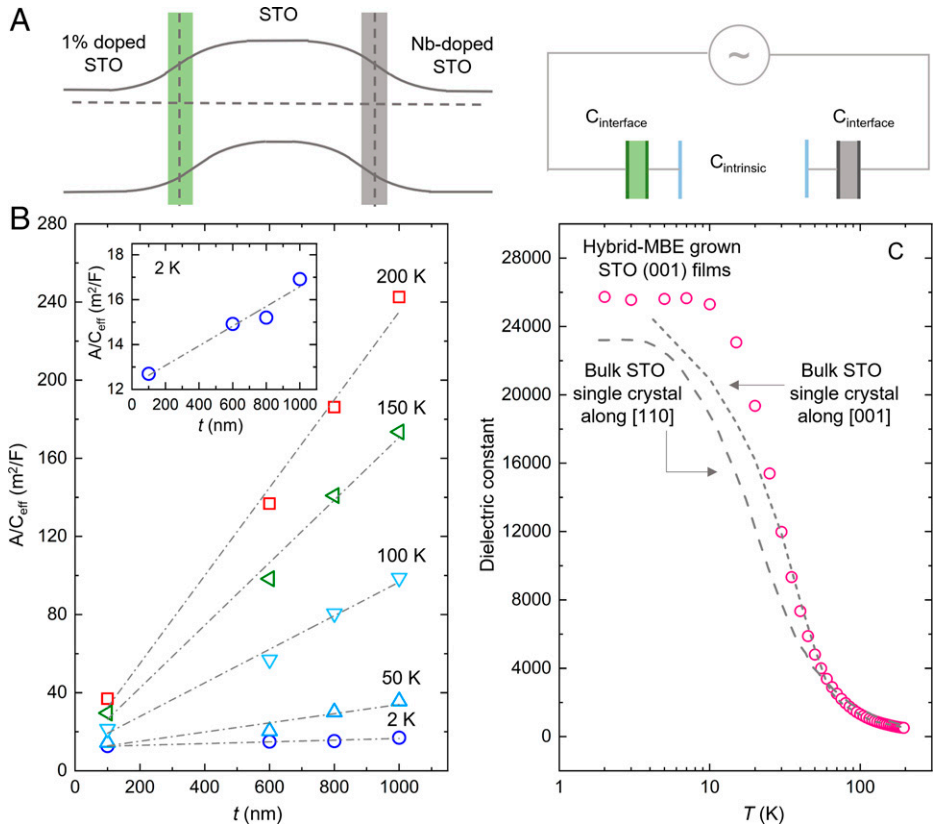

Fig. 3. Band bending at the interfaces and the extracted intrinsic dielectric constant of $SrTiO_3$ films. (*A*) Schematic energy diagram for our capacitor structure (*Left*) and capacitance diagram (*Right*). (*B*) $\frac{A}{C_{eff}}$ as a function of thickness t for the undoped STO film at different temperatures. *Inset* shows $\frac{A}{C_{eff}}$ vs. t at 2 K. All dashed lines are linear fits. (*C*) Extracted intrinsic dielectric constant along the [001] crystallographic direction as a function of temperature. The dashed curves are the bulk STO single-crystal data (1, 3).

as shown in Fig. 2*B*, which also includes data for typical STO bulk single crystals (1,3). Here A is the area of the electrode, t is the thickness of the undoped STO layer, and $\varepsilon_0 = 8.854 \times 10^{-12}$ F/m. As a sanity check, we also plot the measured capacitance as a function of the electrode area for different devices on the same sample (*SI Appendix*, Fig. S1). A linear behavior can be observed, as expected from Eq. **4**, indicating device geometry does not affect the dielectric constant. As shown in Fig. 2*B*, the dielectric constant of the STO film behaves the same as the bulk single crystal above 100 K. Below 100 K, κ starts to deviate from the bulk value and reaches a constant value below ~30 K. At 2 K, the film dielectric constant is ~4,500, which is much smaller than the corresponding bulk value. However, STO thin films grown by hybrid MBE have also been shown to have very low defect densities as evidenced by record high electron mobilities (31). These facts raise an important unanswered question—How can high mobility and low dielectric constant coexist in STO films?

To answer this question, we consider the interfaces between the doped STO electrodes and the undoped STO layer. Carrier spillover from doped STO to undoped STO accompanied by band bending at these interfaces is expected to occur as the Fermi levels equilibrate, as shown schematically in Fig. 3*A*. This can result in layers with different dielectric properties (or dielectric dead layers) forming at the interfaces even without any structural differences at the interface. These two interfacial regions can in principle exhibit different capacitances from that of the undoped STO film and the total measured capacitance will be determined by all three (23, 32), as shown schematically in Fig. 3*A*. The total or effective capacitance measured across the structure consists of the capacitances of the two interfaces and the intrinsic capacitance of the undoped STO film in series:

$$\frac{1}{C_{eff}} = \frac{1}{C_{intrinsic}} + \frac{1}{C_{interface1}} + \frac{1}{C_{interface2}}. \quad [5]$$

If the interfacial capacitance is small, it will dominate the effective capacitance. Inserting Eq. **4**, Eq. **5** becomes

$$\frac{A}{C_{eff}} = \frac{t'}{\kappa_{intrinsic}\varepsilon_0} + \frac{A}{C_{interface}}. \quad [6]$$

Here, t' is the effective thickness of the undoped STO film over which the intrinsic capacitance is operative; note that $t' \approx t$ since the interfacial region width is smaller than the thickness of the undoped layer. We also combine the capacitances from the two interfaces into a single term. Using this model, we argue that by using different thicknesses of the undoped STO layer, we can separate the dielectric constant of the pure, undoped STO film from the interfacial contributions and thus obtain the intrinsic value.

In Fig. 3*B*, we plot $\frac{A}{C_{eff}}$ as a function of film thickness t for the undoped STO films at different temperatures, and linear behavior is clearly observed. Using Eq. **6**, we extract the intrinsic dielectric constants between 2 and 200 K, and these are plotted in Fig. 3*C*. At 2 K, we find that the intrinsic dielectric constant exceeds 25,000, which to the best of our knowledge exceeds the highest bulk single-crystal value measured along the same [001] crystallographic direction previously. The excellent fits of the data to Eq. **6** strongly suggest that the capacitances at the buried interfaces indeed dominate the measured effective capacitance, thereby masking the intrinsic value. A self-consistent check of the model and the assumption that $t' \approx t$ is shown in

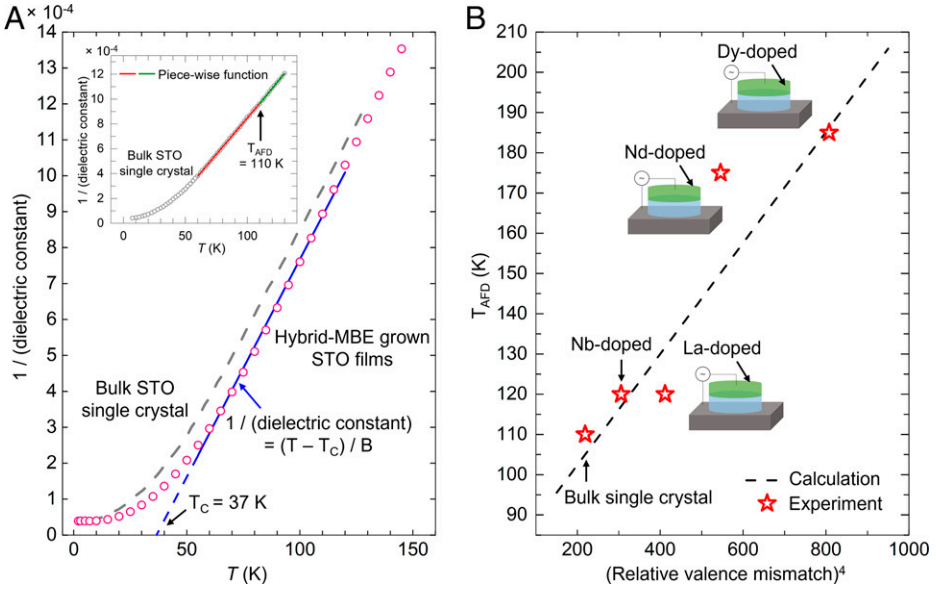

Fig. 4. Curie–Weiss behavior and AFD transition. (*A*) Inverse of the extracted intrinsic dielectric constant as a function of temperature. The blue line is the Curie–Weiss law fit. The dashed line is the bulk single-crystal data (34) for comparison. *Inset* shows the digitalized bulk data with a piecewise function fit. (*B*) Extracted AFD transition temperature as a function of the fourth power of the relative ionic valence mismatch $\langle \varepsilon^4 \rangle$ for the bulk and thin film samples. The dashed line shows the calculated values (35).

SI Appendix, Figs. S2–S4. To understand the origin of low capacitances at the buried interfaces, we calculate the carrier and potential profiles at the *n*-STO/undoped STO interface based on the model proposed in ref. 33. As shown in *SI Appendix*, Fig. S2, an electric field is present at the interface owing to the rearrangement of electrons. As discussed in detail in *SI Appendix*, Figs. S3 and S4, this model further facilitates the determination of the effective dielectric constant at the interface and yields a low temperature value of ∼75. This value is about three orders of magnitude lower than the low-temperature intrinsic value and it dominates the measured capacitance. We further show that the near-surface region in the top electrode does not play a role in generating the low measured capacitance by ruling out the presence of an electronic dead layer via strong upward band bending and surface depletion (see *SI Appendix*, Fig. S5 and related discussion).

In Fig. 4*A*, we plot the inverse of the intrinsic dielectric constant as a function of temperature along with the analogous bulk data (34). Above 60 K, the film plot shows Curie–Weiss behavior similar to that seen in bulk STO, yielding a Curie temperature (T_C) of 37 K, which is comparable to the bulk value (1, 34). In Fig. 4 *A*, *Inset* we also use a piecewise function fit with Eq. 7 on bulk single-crystal data and show a slope change at $T_A = 110$ K:

$$\frac{1}{\kappa} = \frac{T - T_C}{B} \qquad (T < T_A)$$
$$\frac{1}{\kappa} = \frac{T - T_C}{B} + D(T - T_A)\ (T > T_A). \qquad [7]$$

Here, T_A is the transition temperature, and B and D are constants. Such a slope change has been associated with the AFD transition wherein STO undergoes a cubic-to-tetragonal phase transition at 110 K (34). Using the same fitting method along with first derivatives, we observe similar slope changes in our measurements of the effective dielectric constant for samples employing different dopants in the top layer (*SI Appendix*, Figs. S6 and S7). Fig. 4*B* shows the extracted temperatures at which these slope changes occur in our samples. Interestingly, the transition temperature depends on the identity of the dopant in the top electrode. It has been observed that ionic substitutions can shift the AFD transition temperature (T_{AFD}) in STO (35). A unified model (35) has been proposed to describe this shift and the defining formula is

$$\frac{dT_{AFD}}{dx} = \gamma\varepsilon^4 + \eta. \qquad [8]$$

Here, $\frac{dT_{AFD}}{dx}$ is the rate of change of T_{AFD} with respect to the doping density in atomic % (x) and ε is the relative ionic valence mismatch of the substituted cation calculated from bond valence sums with $\gamma = 0.138$ K/at.% and $\eta = -30.2$ K/at.% (35). Based on our measurements, we observe that the temperatures at which the slopes change in plots of $\frac{1}{\kappa}$ vs. T roughly match the expected T_{AFD} values for 1 at.% Nd-, Dy-, and La-doped STO, as illustrated in Fig. 4*B*. This implies that the interface between the top doped layer and the undoped layer affects the measured capacitance. We also note that for all samples, there is another slope change that occurs near 120 K (*SI Appendix*, Figs. S6 and S7). This temperature roughly agrees with the expected T_{AFD} for 0.5 wt% or 1 at.% Nb-doped STO, indicating that there is also a contribution from the interface between the *n*-type substrate and the undoped film. Such agreement suggests that the measured effective capacitance is affected by the interfaces between both electrodes and the undoped STO layer. This result also shows that by observing the slope change in the inverse of the effective dielectric constant as a function of temperature in such capacitor structures, one can quantify the AFD transition temperature for doped STO films as a function of dopant concentration and dopant types. This result further confirms that the *n*-STO/STO interface plays a major role in modifying the effective capacitance across the sample, masking the true value of the intrinsic dielectric constants of STO films.

Conclusion

We have demonstrated that when contributions from the interfaces are taken into account, the intrinsic dielectric constant of homoepitaxially grown STO (001) films reaches over 25,000 at low temperature, exceeding the bulk value in the same crystallographic orientation. Further analysis reveals that signatures of

AFD transitions in both electrodes appear in the measurements, implying that the interfaces between doped STO and the undoped STO affect the effective capacitance. Even when the structure is homoepitaxial, a low capacitance at the buried *n*-STO/undoped STO interface was found and attributed to the presence of an electric field. This work clearly demonstrates that interfacial engineering is a promising approach to tailor the electric field and therefore the dielectric and electronic properties of oxide heterojunctions.

Methods

Growth and Characterization. We use a hybrid MBE (Scienta Omicron Inc.) method (29, 30) to grow 100, 600, 800, and 1,000 nm undoped STO on 0.5 wt% Nb-doped (001) STO substrates and then grow 100 nm of doped STO films in situ for the top electrodes. Dy, Nd, and La were used as dopants and their concentration was fixed at ∼1 at.% of the A sites. All films were grown at 900 °C. RHEED was used to monitor the film growth in situ. High-resolution XRD was carried out after growth to characterize the structure.

Fabrication. After growth, photolithography was used to define patterns on samples. Details about device fabrication are described in *SI Appendix*.

Dielectric Measurement. An impedance analyzer Agilent E4990A is used to measure impedance across the sample as a function of frequency. A Quantum Design PPMS Dynacool system is used for precise temperature control. Calibration of the measurement is detailed in *SI Appendix*.

X-Ray Photoelectron Spectroscopy and UV Photoelectron Spectroscopy Measurement. X-ray photoelectron spectroscopy and UV photoelectron spectroscopy (XPS/UPS) were carried out at ambient temperature with an Omicron Scienta R3000 analyzer having a 30° acceptance cone. Monochromatic Al Kα X-rays ($h\upsilon$ = 1,487 eV), a 100-eV pass energy, and a 0.8-mm slit width were used for XPS. The resulting energy resolution was ∼400 meV as judged by fitting the Fermi edge for a clean, polycrystalline Ag foil to the Fermi–Dirac function. Monochromatic He I VUV light ($h\upsilon$ = 21.2 eV), a pass energy of 10 eV, and a 0.8-mm slit were used for UPS, resulting in an energy resolution of ∼60 meV, determined as described above. All spectra were measured at normal emission. There was no evidence of surface charging in either XPS or UPS. The binding-energy scales were calibrated using the Ag $3d_{5/2}$ core level (368.21 eV) and the Ag Fermi level for a clean, polycrystalline Ag foil.

Hard X-Ray Photoelectron Spectroscopy Measurement. Hard X-ray photoelectron spectroscopy (HAXPES) measurements were made at the Diamond Light Source (United Kingdom) on Beamline I09. X-ray energies were selected using a Si(111) double-crystal monochromator followed by a Si(004) channel-cut high-resolution monochromator. A Scienta Omicron EW4000 high-energy hemispherical analyzer was set to a 200-eV pass energy, resulting in an overall experimental resolution of ∼250 meV, as judged using the method described in the previous paragraph. No charging was observed in HAXPES. The binding-energy scale was calibrated using the Fermi edge of a gold foil.

Data Availability. All study data are included in this article and/or *SI Appendix*.

ACKNOWLEDGMENTS. We thank Boris Shklovskii and Yi Huang for useful discussions. This work was primarily supported by the Air Force Office of Scientific Research through Grant FA9550-21-1-0025 and National Science Foundation (NSF) through the Materials Research Science and Engineering Centers (MRSEC) program under Award DMR-2011401. This work is also partially supported by the Vannevar Bush Faculty Fellowship and by the NSF through DMR-1741801. MBE growth was supported by the US Department of Energy (DOE) through Grant DE-SC002021. Parts of this work were carried out at the Characterization Facility, University of Minnesota, which receives partial support from the NSF through the MRSEC program under Award DMR-2011401. Device fabrication was carried out at the Minnesota Nano Center, which is supported by the NSF through the National Nano Coordinated Infrastructure under Award ECCS-1542202. The work at Pacific Northwest National Laboratory was supported by the US DOE, Office of Science, Division of Materials Sciences and Engineering under Award 10122.

Author affiliations: [a]Department of Chemical Engineering and Materials Science, University of Minnesota, Twin Cities, Minneapolis, MN 55455; [b]School of Physics and Astronomy, University of Minnesota, Twin Cities, Minneapolis, MN 55455; [c]Diamond Light Source, Ltd., Didcot, Oxfordshire OX11 0DE, United Kingdom; [d]Aerospace Engineering and Mechanics, University of Minnesota, Twin Cities, Minneapolis, MN 55455; and [e]Physical and Computational Sciences Directorate, Pacific Northwest National Laboratory, Richland, WA 99352

1. K. A. Müller, H. Burkard, $SrTiO_3$: An intrinsic quantum paraelectric below 4 K. *Phys. Rev. B* **19**, 3593–3602 (1979).
2. O. E. Kvyatkovskii, Quantum effects in incipient and low-temperature ferroelectrics (a review). *Phys. Solid State* **43**, 1401–1419 (2001).
3. R. C. Neville, B. Hoeneisen, C. A. Mead, Permittivity of strontium titanate. *J. Appl. Phys.* **43**, 2124 (1972).
4. A. Spinelli, M. A. Torija, C. Liu, C. Jan, C. Leighton, Electronic transport in doped $SrTiO_3$: Conduction mechanisms and potential applications. *Phys. Rev. B* **81**, 155110 (2010).
5. X. Lin, Z. Zhu, B. Fauqué, K. Behnia, Fermi surface of the most dilute superconductor. *Phys. Rev. X* **3**, 021002 (2013).
6. O. N. Tufte, P. W. Chapman, Electron mobility in semiconducting strontium titanate. *Phys. Rev.* **155**, 796 (1967).
7. X. Lin *et al.*, Critical doping for the onset of a two-band superconducting ground state in $SrTiO_{3-\delta}$. *Phys. Rev. Lett.* **112**, 207002 (2014).
8. S. Hameed *et al.*, Enhanced superconductivity and ferroelectric quantum criticality in plastically deformed strontium titanate. *Nat. Mater.* **21**, 54–61 (2022).
9. J. H. Haeni *et al.*, Room-temperature ferroelectricity in strained $SrTiO_3$. *Nature* **430**, 758–761 (2004).
10. S. Salmani-Rezaie, K. Ahadi, W. M. Strickland, S. Stemmer, Order-disorder ferroelectric transition of strained $SrTiO_3$. *Phys. Rev. Lett.* **125**, 087601 (2020).
11. A. Verma, S. Raghavan, S. Stemmer, D. Jena, Ferroelectric transition in compressively strained $SrTiO_3$ thin films. *Appl. Phys. Lett.* **107**, 192908 (2015).
12. R. Wördenweber, E. Hollmann, R. Kutzner, J. Schubert, Induced ferroelectricity in strained epitaxial $SrTiO_3$ films on various substrates. *J. Appl. Phys.* **102**, 044119 (2007).
13. K. Ahadi *et al.*, Enhancing superconductivity in $SrTiO_3$ films with strain. *Sci. Adv.* **5**, eaaw0120 (2019).
14. P. A. Fleury, J. F. Scott, J. M. Worlock, Soft phonon modes and the 110°K phase transition in $SrTiO_3$. *Phys. Rev. Lett.* **21**, 16–19 (1968).
15. A. Yamanaka *et al.*, Evidence for competing orderings in strontium titanate from hyper-Raman scattering spectroscopy. *Europhys. Lett.* **50**, 688–694 (2000).
16. M. Gabay, J.-M. Triscone, Ferroelectricity woos pairing. *Nat. Phys.* **13**, 624–625 (2017).
17. C. W. Rischau *et al.*, A ferroelectric quantum phase transition inside the superconducting dome of $Sr_{1-x}Ca_xTiO_{3-\delta}$. *Nat. Phys.* **13**, 643–648 (2017).
18. R. Russell *et al.*, Ferroelectric enhancement of superconductivity in compressively strained $SrTiO_3$ films. *Phys. Rev. Mater.* **3**, 091401 (2019).
19. Y. Tomioka, N. Shirakawa, K. Shibuya, I. H. Inoue, Enhanced superconductivity close to a non-magnetic quantum critical point in electron-doped strontium titanate. *Nat. Commun.* **10**, 738 (2019).
20. J. H. Hao, Z. Luo, J. Gao, Effects of substrate on the dielectric and tunable properties of epitaxial $SrTiO_3$ thin films. *J. Appl. Phys.* **100**, 114107 (2006).
21. F. He *et al.*, Anomalous phase transition in strained $SrTiO_3$ thin films. *Appl. Phys. Lett.* **83**, 123–125 (2003).
22. B. Kim *et al.*, Dielectric properties of sub 20 nm homoepitaxial $SrTiO_3$ thin film grown by molecular beam epitaxy using oxygen plasma. *Ferroelectrics* **571**, 76–84 (2021).
23. H.-C. Li, W. Si, A. D. West, X. X. Xi, Thickness dependence of dielectric loss in $SrTiO_3$ thin films. *Appl. Phys. Lett.* **73**, 464–466 (1998).
24. M. Lippmaa *et al.*, Step-flow growth of $SrTiO_3$ thin films with a dielectric constant exceeding 10^4. *Appl. Phys. Lett.* **74**, 3543–3545 (1999).
25. H.-C. Li *et al.*, Dielectric properties of $SrTiO_3$ thin films grown on various perovskite electrodes by pulsed laser deposition. *Mater. Sci. Eng. B* **56**, 218–222 (1998).
26. H. Takashima, M. Cho, T. Taniyama, M. Itoh, Surface morphology and dielectric behavior of perovskite $SrTiO_3$ thin film in heterostructure electroluminescence devices. *Curr. Appl. Phys.* **17**, 657–660 (2017).
27. H. Takashima, R. Wang, M. Okano, A. Shoji, M. Itoh, Structure and dielectric behavior of epitaxially grown $SrTiO_3$ film between $YBa_2Cu_3O_{7-\delta}$ electrodes. *Jpn. J. Appl. Phys.* **43**, L170–L172 (2004).
28. H. Takashima, R. Wang, B. Prijamboedi, A. Shoji, M. Itoh, Frequency dependence of dielectric constant of strontium titanate films with single-crystal-like behavior. *Ferroelectrics* **335**, 45–50 (2006).
29. B. Jalan, R. Engel-Herbert, N. J. Wright, S. Stemmer, Growth of high-quality $SrTiO_3$ films using a hybrid molecular beam epitaxy approach. *J. Vac. Sci. Technol. A* **27**, 461–464 (2009).
30. B. Jalan, P. Moetakef, S. Stemmer, Molecular beam epitaxy of $SrTiO_3$ with a growth window. *Appl. Phys. Lett.* **95**, 032906 (2009).
31. J. Son *et al.*, Epitaxial $SrTiO_3$ films with electron mobilities exceeding 30,000 $cm^2 V^{-1} s^{-1}$. *Nat. Mater.* **9**, 482–484 (2010).
32. M. Stengel, N. A. Spaldin, Origin of the dielectric dead layer in nanoscale capacitors. *Nature* **443**, 679–682 (2006).
33. H. Fu, K. V. Reich, B. I. Shklovskii, Electron gas induced in $SrTiO_3$. *J. Exp. Theor. Phys.* **122**, 456–471 (2016).
34. T. Sakudo, H. Unoki, Dielectric properties of $SrTiO_3$ at low temperatures. *Phys. Rev. Lett.* **26**, 851 (1971).
35. E. McCalla, J. Walter, C. Leighton, A unified view of the substitution-dependent antiferrodistortive phase transition in $SrTiO_3$. *Chem. Mater.* **28**, 7973–7981 (2016).